Mechie, J., Zhao, W., Karplus, M. S., Wu, Z., Meissner, R., Shi, D., Klemperer, S. L., Su, H., Kind, R., Xue, G., Brown, L. D. (2012): Crustal shear (S) velocity and Poisson's ratio structure along the INDEPTH IV profile in northeast Tibet as derived from wide-angle seismic data. - Geophysical Journal International, 191, 2, pp. 369—384.

DOI: http://doi.org/10.1111/j.1365-246X.2012.05616.x

Geophysical Journal International

Geophys. J. Int. (2012) **191,** 369–384 doi: 10.1111/j.1365-246X.2012.05616.x

Crustal shear (*S*) velocity and Poisson's ratio structure along the INDEPTH IV profile in northeast Tibet as derived from wide-angle seismic data

J. Mechie,[1] W. Zhao,[2] M. S. Karplus,[3] Z. Wu,[2] R. Meissner,[4] D. Shi,[2] S. L. Klemperer,[3] H. Su,[2] R. Kind,[1,5] G. Xue[2] and L. D. Brown[6]

[1] *Deutsches GeoForschungsZentrum—GFZ, Sections "Geophysical Deep Sounding" and "Seismology", Telegrafenberg,* 14473 *Potsdam, Germany. E-mail: jimmy@gfz-potsdam.de*
[2] *Chinese Academy of Geological Sciences,* 26 *Baiwanzhuang Road, Beijing,* 100037*, China*
[3] *Department of Geophysics, Stanford University,* 397 *Panama Mall, Mitchell Building 360, Stanford, CA* 94305*, United States*
[4] *Institute of Geosciences, Christian Albrechts University, Otto-Hahn-Platz* 1, 24118*, Kiel, Germany*
[5] *Institut für Geologische Wissenschaften, Freie Universität Berlin,* 12249 *Berlin, Germany*
[6] *Department of Earth and Atmospheric Sciences,* 3120 *Snee Hall, Cornell University, Ithaca, NY* 14853*, United States*

Accepted 2012 July 19. Received 2012 June 20; in original form 2012 March 5

SUMMARY

From the *S*-wave data collected along a 270-km-long profile spanning the Kunlun mountains in NE Tibet, 14595 *Sg* phase arrivals and 21 *SmS* phase arrivals were utilized to derive a whole-crustal *S* velocity model and, together with a previously derived *P* velocity model, a Poisson's ratio (σ) model beneath the profile. The final tomogram for the upper 10–15 km of the crust reveals the lower velocities associated with the predominantly Neogene-Quaternary sediments of the Qaidam basin to the north and the higher velocities associated with the predominantly Palaeozoic and Mesozoic upper crustal sequences of the Songpan-Ganzi terrane and Kunlun mountains to the south. This study finds no evidence that the Kunlun mountains are involved in large-scale northward overriding of the Qaidam basin along a shallow south-dipping thrust. The σ in the upper 10–15 km of the crust are often lower than 0.25, indicating a preponderance of quartz-rich rocks in the upper crust beneath the profile. Below 10–15 km depth, the remainder of the crust down to the Moho has an average σ of 0.24 beneath the Songpan-Ganzi terrane and Kunlun mountains and 0.25 below the Qaidam basin. These low σ are similar to other low σ found along other profiles in the northeastern part of the plateau. Assuming an isotropic situation and no significant variation in σ between 10–15 km depth and the Moho, then the lower crust between 25–30 km depth below sea level and the Moho with *P* velocities varying from 6.6 km s^{-1} at the top to around 6.9 km s^{-1} at the base and σ of 0.24–0.25 should comprise intermediate granulites in the upper part transitioning to granulite facies metapelites in the lower part. As the pre-Cenozoic Qaidam basin crust has probably not lost any of its lower crust during the present Himalayan orogenic cycle in the Cenozoic and only has a σ of 0.245–0.25, then it appears that the pre-Cenozoic Qaidam basin crust involved in the collision is more felsic and thus weaker and more easily deformable than normal continental crust with a global average σ of 0.265–0.27 and the Tarim and Sichuan basin crusts. This situation then probably facilitates the collision and promotes the formation of new high plateau crust at the NE margin of Tibet. South of the Qaidam basin, the crust of the Songpan-Ganzi terrane and Kunlun mountains has an even lower average crustal σ of 0.23–0.24 and is thus presumably even weaker and more easily deformable than the crust beneath the Qaidam basin. This then supports the hypothesis of Karplus *et al.* that 'the high Tibetan Plateau may be thickening northward into south Qaidam as its weak, thickened lower crust is injected beneath stronger Qaidam crust'.

Key words: Continental tectonics: compressional; Crustal structure; Asia.

INTRODUCTION AND GEOLOGY

During the International Deep Profiling of Tibet and the Himalaya (INDEPTH) phase IV controlled-source seismic experiment in 2007 June, 949 vertical-component seismographs (IRIS-PASSCAL Texans) at 100–650 m station spacing and 20 broad-band and 29 short-period three-component seismographs (34 from GIPP, Germany and 15 from SEIS-UK) at 5–6 km station spacing recorded five large shots (1000–2000 kg) and 102 small shots (60–240 kg) along a 270-km-long profile across the Kunlun mountains from the Songpan-Ganzi terrane to the Qaidam basin (Fig. 1). Following the controlled-source seismic experiment the three-component seismographs were partly redeployed such that 24 broad-band seismographs occupied the central part of the 270-km-long profile across the Kunlun mountains between shots KS2 and KS4 and the other 26 broad-band seismographs extended along a profile across the Jinsha suture between shot KS3 and Tuotuo. This deployment of 50 broad-band seismographs to record earthquakes lasted until 2008 September. During the recording period, two local earthquakes about 50 km south of the south end of the controlled-source profile were recorded. The two earthquakes were just in the correct place to provide valuable information on both the compressional (*P*) and shear

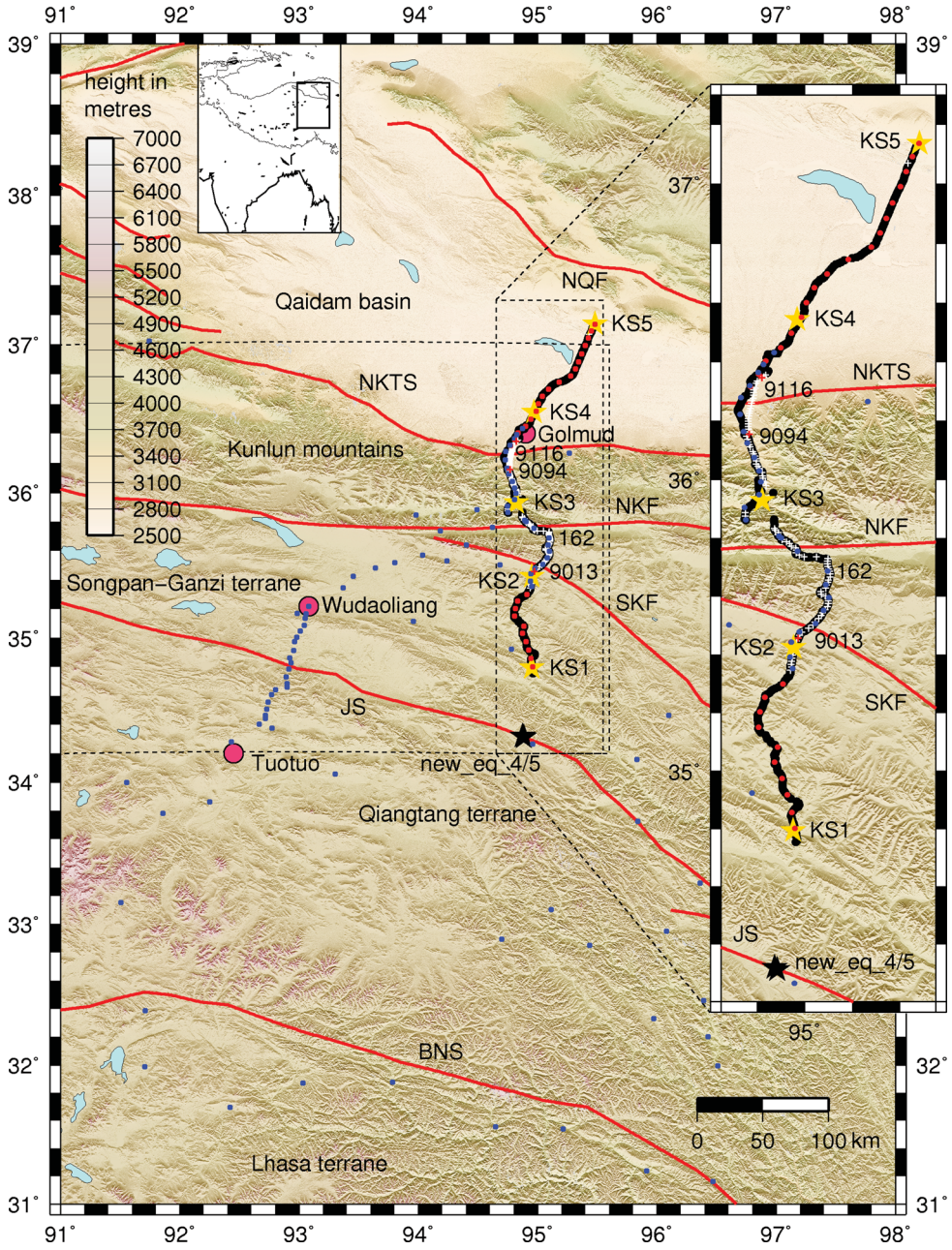

Figure 1. Location map (box within the inset) with events (shots and earthquakes) and stations. The larger dashed black box shows the area covered by Fig. 2 and the smaller dashed black box shows the area covered in more detail to the right. Key: Gold stars, large shots; small white crosses, small shots; small red crosses, small shots 9013, 9094 and 9116, for which data are shown; black stars, local earthquakes; black dots, one-component recorders; red dots, three-component short-period recorders; blue dots, three-component broad-band recorders; NQF, North Qaidam Fault; NKTS, North Kunlun Thrust System; NKF, North Kunlun Fault; SKF, South Kunlun Fault; JS, Jinsha Suture; BNS, Banggong-Nujiang Suture. In the inset the outline of the Tibet plateau, as defined by the 3000 m contour, is shown.

(*S*) velocities to supplement the information gained from the shots along the controlled-source profile. It was also possible to relocate these two events as the profiles were supplemented by a 2-D array of broad-band three-component seismographs (Wei *et al.* 2010). The relocation was accomplished utilizing the HYPO71PC computer program (Lee & Valdés 1985) and a local 1-D *P* velocity model, based on an average of an early version of the 2-D *P* velocity model along the controlled-source profile (Karplus *et al.* 2011).

The 2-D *P* velocity model (Karplus *et al.* 2011) delineated the *P* velocity structure and major layer boundaries, for example Moho beneath the controlled-source profile. This model provided new detail on the geometry of the Moho step between the approximately 70-km-thick crust of the Songpan-Ganzi terrane and the approximately 50-km-thick crust of the Qaidam basin. The observation of overlapping Mohos at about 50 and 70 km depth beneath the southernmost 40 km of the Qaidam basin led Karplus *et al.* (2011) to the hypothesis that the high Tibetan plateau grows northwards as weak crust from the Songpan-Ganzi terrane injects beneath the stronger crust of the Qaidam basin. The main aim of this study is to derive a 2-D *S* velocity model beneath the controlled-source profile and then, using this model and the *P* velocity model of Karplus *et al.* (2011), to derive a 2-D Poisson's ratio (σ) model beneath the profile. This should better delineate the physical properties and thus the rock types below the profile (Holbrook *et al.* 1992) which, in turn, should allow some evaluation of the hypothesis of Karplus *et al.* (2011) regarding the injection of weak Songpan-Ganzi crust beneath the stronger crust of the Qaidam basin. Previous seismic studies in the region have provided evidence for rather low σ, both for the whole crust and the lower crust (Kind *et al.* 2002; Vergne *et al.* 2002; Galvé *et al.* 2006; Jiang *et al.* 2006; Yue *et al.* 2012). Jiang *et al.* (2006) invoked anisotropy as a possible explanation for a very low value for σ of 0.20 in the lower crust of the Songpan-Ganzi terrane along a profile in NE Tibet about 300 km southeast of the INDEPTH IV profile. Hence the results of this study are compared with the results of the previous studies and an attempt is made to provide an explanation in terms of possible rock types for the low σ especially in the lower crust.

The southern half of the controlled-source profile crosses predominantly the Triassic rocks of the Songpan-Ganzi flysch (Fig. 2), thought to have a thickness in excess of 10 km and locally up to 15 km (Weislogel 2008). Karplus *et al.* (2011) concluded that the flysch deposits are 8–14 km thick beneath the controlled-source profile, based on interpretation of the *P* traveltime data. The southern half of the profile also crosses the major left-lateral strike-slip South Kunlun Fault (SKF) and North Kunlun Fault (NKF), the latter marking in the area of the INDEPTH IV profile the site of the Palaeozoic Anyimaqen-Kunlun-Muztagh suture (Molnar *et al.* 1987; Yin & Harrison 2000). The valleys along which both these faults run are filled with recent alluvium and moraine, predominantly on the south sides of the faults (Fig. 2). The northern half of the profile crosses, from the south, mainly Ordovician carbonates and phyllites, followed by Devonian volcanics, the predominantly Permo-Triassic granodiorites of the north Kunlun batholith and, finally, north of the North Kunlun Thrust System (NKTS) the Quaternary deposits of the Qaidam basin. The NKTS has been invoked to accommodate shortening in NE Tibet and uplift of the Kunlun Mountains caused by the India–Eurasia collision (Kidd *et al.* 1988; Burchfiel *et al.* 1989; Mock *et al.* 1999). Where the INDEPTH IV profile intersects the NKTS, recent alluvial deposits prevent any direct observation of a fault trace. As a similar situation occurs over much of the length of the NKTS, Yin *et al.* (2007) doubt the existence of a north-vergent NKTS. Indeed, in the Kunlun mountains south-vergent thrust faults of Cenozoic age have been identified (Fig. 2; Yin *et al.* 2007; Wu *et al.* 2009). At about the longitude of Golmud, the sediments of the Qaidam basin, which range in age from Palaeocene to Quaternary, reach a total thickness of about 8 km approximately in the middle of the basin and thin southward to about 2 km near the southern edge of the basin (Yin *et al.* 2008). The southward thinning of the basin means that it cannot just be a simple foreland basin in front of the Kunlun mountains (Bally *et al.* 1986). Based on modelling of the *P* traveltime data, Karplus *et al.* (2011) concluded that beneath the controlled-source profile where it crosses the Qaidam basin, about 4 km of Cenozoic sediments overlie about 4 km of Mesozoic and/or Palaeozoic sedimentary rocks.

DATA AND PHASE CORRELATIONS

Within the *S* wavefield two phases could be recognized. The first of these is the *Sg* phase, which is the direct or refracted *S* wave through the upper crust. The second is the *SmS* phase which is the *S*-wave reflection from the Moho. The *Sg* phase could be picked on the record sections from all but two (numbers 9103 and 9119) of the shots (Fig. 3). To guide the picking of the *Sg* phase, firstly, both the *Pg* (direct or refracted *P* wave through the upper crust) and *Sg* phases were picked on the three-component data. The *Pg* phase was picked on the vertical component and the *Sg* phase was picked on the horizontal components. The picking was also done on receiver gathers (e.g. Fig. 3b) as there were fewer three-component stations than shots. Uncertainty estimates of either ± 0.05, ± 0.1 or ± 0.2 s were assigned individually to each pick. Then the picks were reordered into the shot domain and the *Sg* phase was picked in the shot gathers of the vertical-component data of the Texan instruments. In this step the picks from the three-component data were used as a framework to guide the picking of the vertical-component data of the Texan instruments. Uncertainty estimates of either ± 0.05, ± 0.1 or ± 0.2 s were determined automatically, depending on source–receiver distance and on how well the phase could be followed from one trace to the next. This resulted in a total of 15188 picks for the *Sg* phase, which could be picked in some cases out to distances in excess of 60 km (Figs 3a–e). After determining the ratio between the *Sg* phase traveltimes (t_S) and the *Pg* phase traveltimes (t_P), *Sg* phase traveltimes for which t_S/t_P was either less than 1.6 or greater than 2.4 were rejected. The application of this criterion helps to avoid two pitfalls when picking the *Sg* phase. The first of these pitfalls is the danger of picking the surface wave instead of the *Sg* phase. This can be seen in the data for shot 9116 (Fig. 3e) where the picks beyond about 3 km distance north of the shotpoint probably belong to the surface wave phase and not the *Sg* phase. The second pitfall is the danger of picking *S* to *P* converted phases especially when trying to pick the *Sg* phase on the single, vertical-component Texan data. Such phases are prominent in the data for shot KS3 (Fig. 3c), emerging in front of the *Sg* phase and travelling with about the same apparent velocity as the *Pg* phase. They can also be observed in the data for shots 9013 (Fig. 3a) and 9094 (Fig. 3d) and also at about 80 km distance south of shot 9116 (Fig. 3e). Following the rejection of the *Sg* phase traveltimes for which t_S/t_P was either too small or too large, there were 14595 picks left for the *Sg* phase. These 14595 *Sg* picks then formed the basic data set which was tomographically inverted to derive a *S* velocity model for the upper crust beneath the INDEPTH IV profile. The root mean square (rms) of the assigned traveltime uncertainties for the 14595 *Sg* picks is ± 0.18 s.

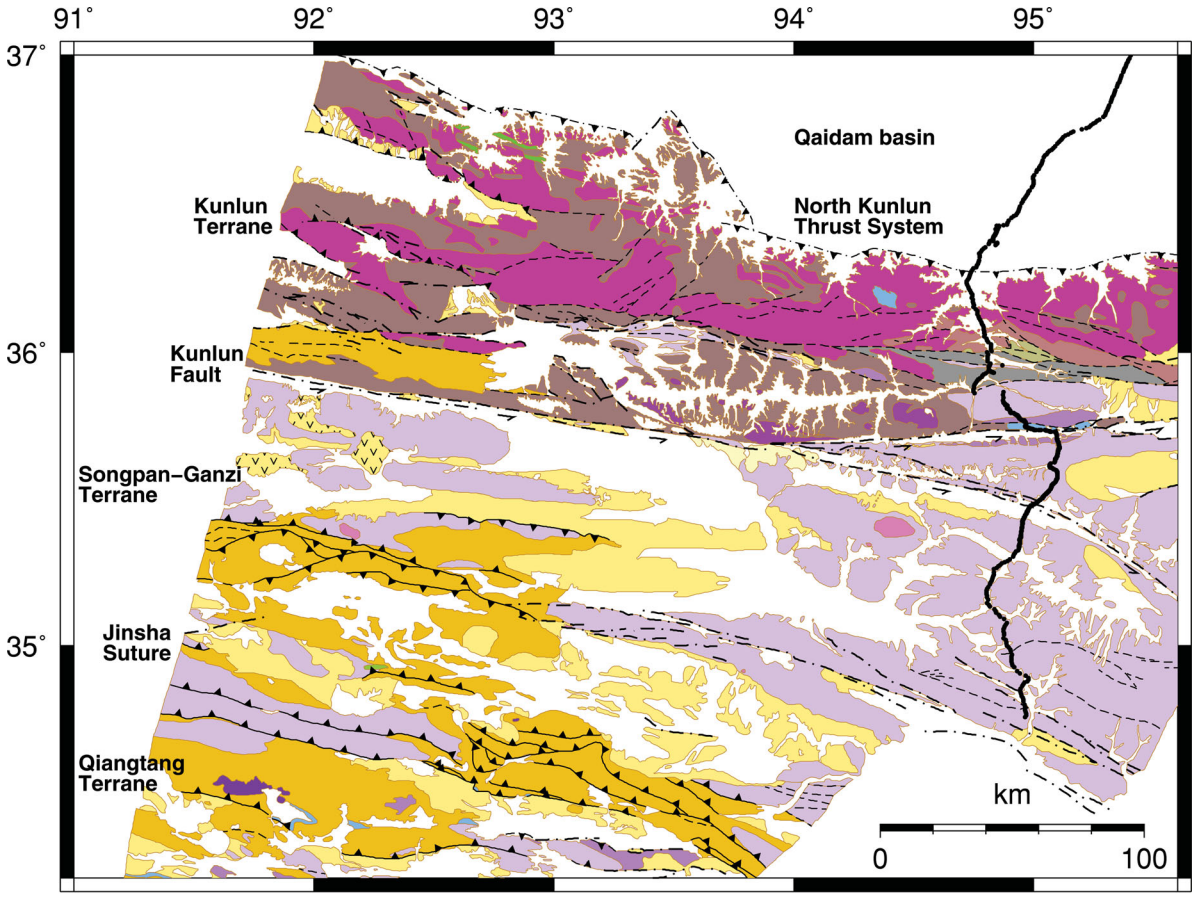

Faults are represented by full, dashed or dashed–dotted lines. The sense of movement (reverse or strike–slip) is indicated, if known, by triangles or half–arrows. Faults represented by dashed–dotted lines have a probable late Neogene or Quaternary movement. All other faults are of unspecified age, but where the sense of movement is known the fault is represented by a full line, otherwise it is represented by a dashed line.

Qiangtang Terrane	Songpan–Ganzi Terrane	Kunlun Terrane
Intrusives		
syenite (Tertiary) Qiangt. Terr. granitoids (late Jurassic)	granites (late Triassic)	gabbro granitoid rocks (early Jurassic) N. Kunlun bathol. (mainl. Perm.–Tria.)
Mainly sediments and extrusives		
alluvium, moraine, etc. (recent) sand, grav., marl, lake beds (Neog.) red arenite, siltst., congl. (Palaeogene) arenite, siltst., shale, limest. (Jurassic) arenite, limestone, shale, coal (Trias.) clastics, bimodal volc., limest. (Perm.) shale, volcanics (Carboniferous)	alluvium, moraine, etc. (recent) moraine, gravel, lake beds (Quatern.) sand, grav., marl, lake b.,v–volc.(Neo.) red arenite, siltst., congl. (Palaeogene) slate, phyllite, aren.–flysch (Triassic) gabbro & ultramafic rocks (Triassic)	alluvium, moraine, etc. (recent) sand, gravel, marl, lake beds (Neog.) red arenite, siltst., congl. (Palaeogene) green & red arenite, shale (Jurassic) green arenite, congl., limest. (Triassic) limestone, shale (Permian) red arenite, shale, limest. (Carbonif.) andesite–rhyolite volc. (Devonian) carbonates, phyllite (Ordovician) phyllite, arenite, mafic volc. (Palaeoz.)

Figure 2. Geological map of northern Tibet after Kidd *et al.* (1988). The black line marks the location of the INDEPTH IV controlled-source seismic profile.

The *SmS* phase, the second phase which can be identified in the *S* wavefield of the INDEPTH IV seismic data, can locally be observed in the data from shot KS5 (Fig. 4) and thus the average crustal σ beneath the Qaidam basin is quite well constrained. The phase is best observed in the data from the horizontal components between 110 and 130 km distance (Fig. 4), but it can also be observed on the single, vertical-component Texan data in the same distance range. The *SmS* phase can also be recognized, although not quite

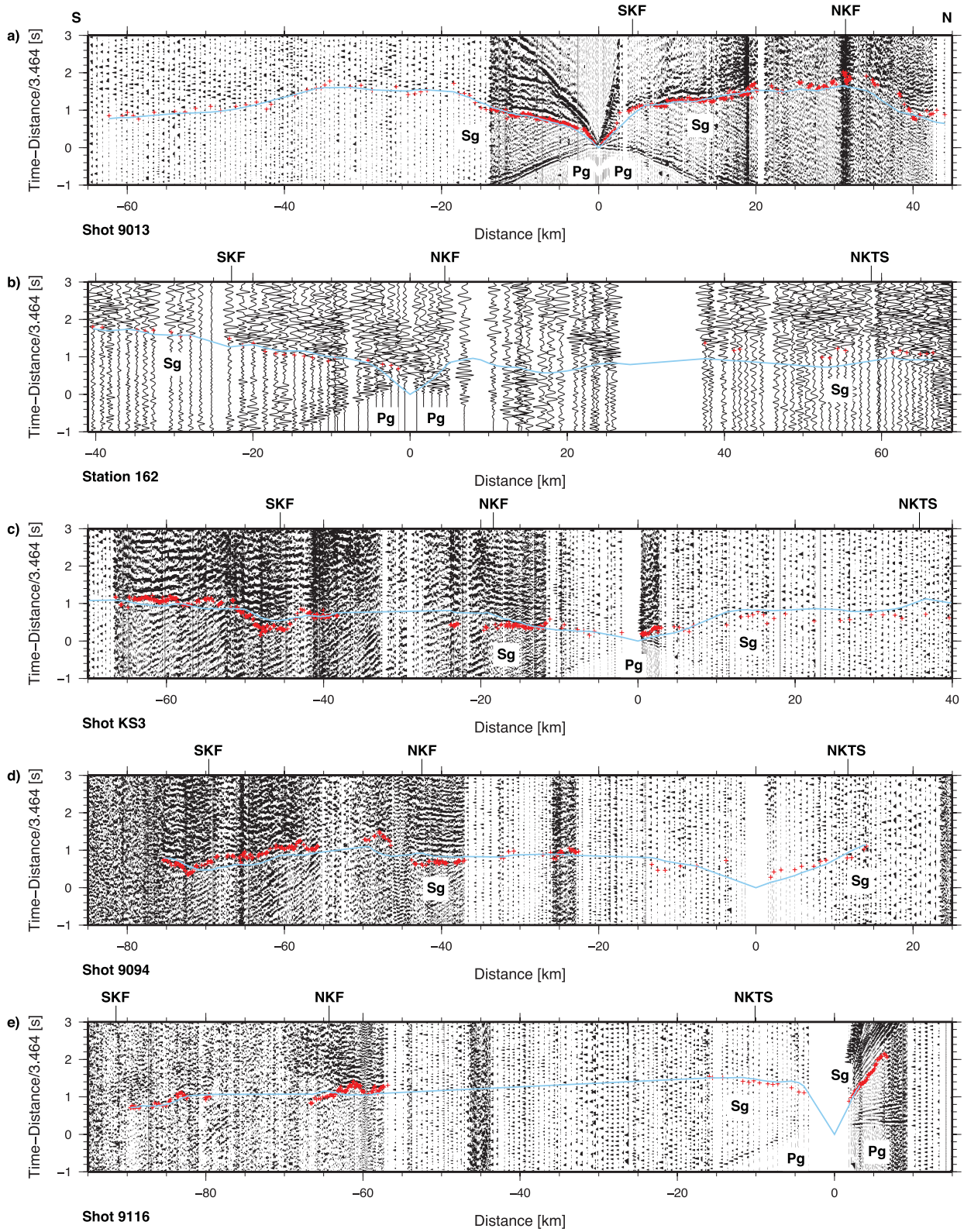

Figure 3. Seismic data from (a) shot 9013, (b) station 162, (c) shot KS3, (d) shot 9094 and (e) shot 9116. The record sections show the vertical component of *S*-wave motion, except for (b) which shows the E–W horizontal (approximately transverse) component of *S*-wave motion, reduced with a velocity of 3.46 km s^{-1}. Each trace is normalized individually and bandpass filtered from 2–12 Hz (a, b, d and e) or 2–10 Hz (c). Blue lines represent phases calculated from the model in Fig. 6(b), and red crosses represent picked traveltimes. In (e) the red crosses N of the end of the blue line represent picked traveltimes which were not included in the inversion (see also discussion in text). Key: see Fig. 1 and *Pg*, first arrival *P*-wave refraction through the upper crust; *Sg*, *S*-wave refraction through the upper crust.

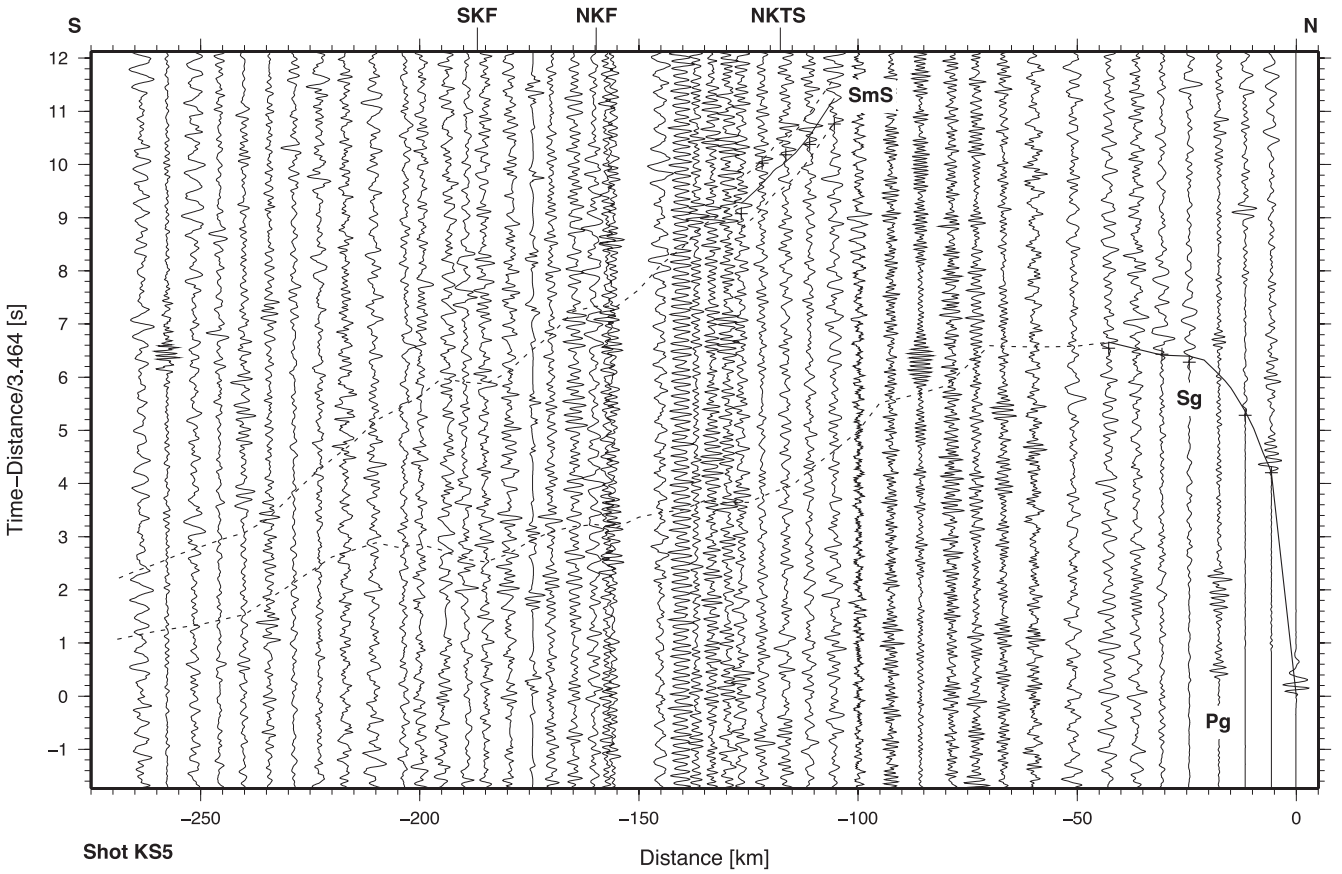

Figure 4. Seismic data from shot KS5 recorded along the INDEPTH IV profile. The record section shows the E–W horizontal (approximately transverse) component of *S*-wave motion reduced with a velocity of 3.46 km s^{-1}. Each trace is normalized individually and bandpass filtered from 2–10 Hz. Lines represent phases calculated from the model in Fig. 9, whereas crosses represent observed traveltimes. Beyond the regions where observed traveltimes exist, the theoretical phases are shown as dashed lines. Dashed lines sub-parallel to the solid line for the *SmS* phase indicate traveltimes if the average Poisson's ratio for the region between 6–9 km depth b.s.l. and the Moho (Fig. 9) is changed from 0.25 to either 0.24 (earlier line) or 0.26 (later line). Key: see Figs 1 and 3 and *SmS*, *S*-wave reflection from the Moho.

so well, in the horizontal-component data from events new_eq_4 and new_eq_5 (Fig. 5), about 50 km south of the south end of the INDEPTH IV controlled-source seismic profile. In this case, the phase can be observed at distances beyond about 200 km and thus the average crustal σ beneath the Songpan-Ganzi terrane and Kunlun mountains can also be constrained, although not quite as confidently as below the Qaidam basin. The rms of the assigned traveltime uncertainties for the 21 *SmS* picks is $\pm$0.20 s.

MODELLING

Upper crust

To derive a 2-D *S* velocity model for the upper 20 km of the crust, the 14595 *Sg* traveltimes were inverted using tomographic methods. The forward part of the tomographic problem was solved by tracing rays through the medium on a 50-m grid using a finite-differences approximation of the eikonal equation (Vidale 1988; Podvin & Lecomte 1991; Schneider *et al.* 1992). As the shot and receiver distribution along the INDEPTH IV profile was very inhomogeneous, the node distribution at which velocities were to be solved was also inhomogeneous. Between profile kilometres 70 and 170 where the shot spacing was 1 km and the receiver spacing was 100–650 m, the horizontal node spacing was 2 km. To the south where there was only the shot KS1 at the southern end of the profile and where the receiver spacing was 650 m, the horizontal node spacing was 5 km. To the north where there were the shots KS4, 9119 (small shot 8 km S of shot KS5) and KS5 and where the receiver spacing was again 650 m, the horizontal node spacing was 5–20 km. Also the vertical node spacing was varied, with 1 km spacing in the uppermost 2 km, 2 km in the next 6 km, 3 km in the next 6 km and then 4 km. Partial derivatives of the calculated traveltimes with respect to the velocity nodes were derived utilizing the techniques described by Lutter *et al.* (1990) and Zelt & Smith (1992). The inverse part of the problem was solved by damped least-squares inversion (see e.g. Zelt & Smith 1992; Zelt & Barton 1998), in which an overall damping factor of 1000 was employed. The resulting velocity-node updates were added to the already existing velocity values and the forward and inverse problems were carried out again until a suitable convergence between the observed and calculated traveltimes was obtained. The tomographic algorithms and node separation used in this study for the *S*-wave data are the same as those used by Karplus *et al.* (2011) for the *P*-wave data.

Because of the paucity of *Sg* traveltime picks from the Qaidam basin, it was not possible to use a 1-D laterally homogeneous initial model to derive a 2-D *S* velocity model for the upper 20 km of the crust. Thus a 1-D initial model for the Qaidam basin was derived using the few ($\sim$110) picks from the Qaidam basin, from shots KS4 and KS5. From the many picks from the remainder of the profile, south of the Qaidam basin, another 1-D initial model

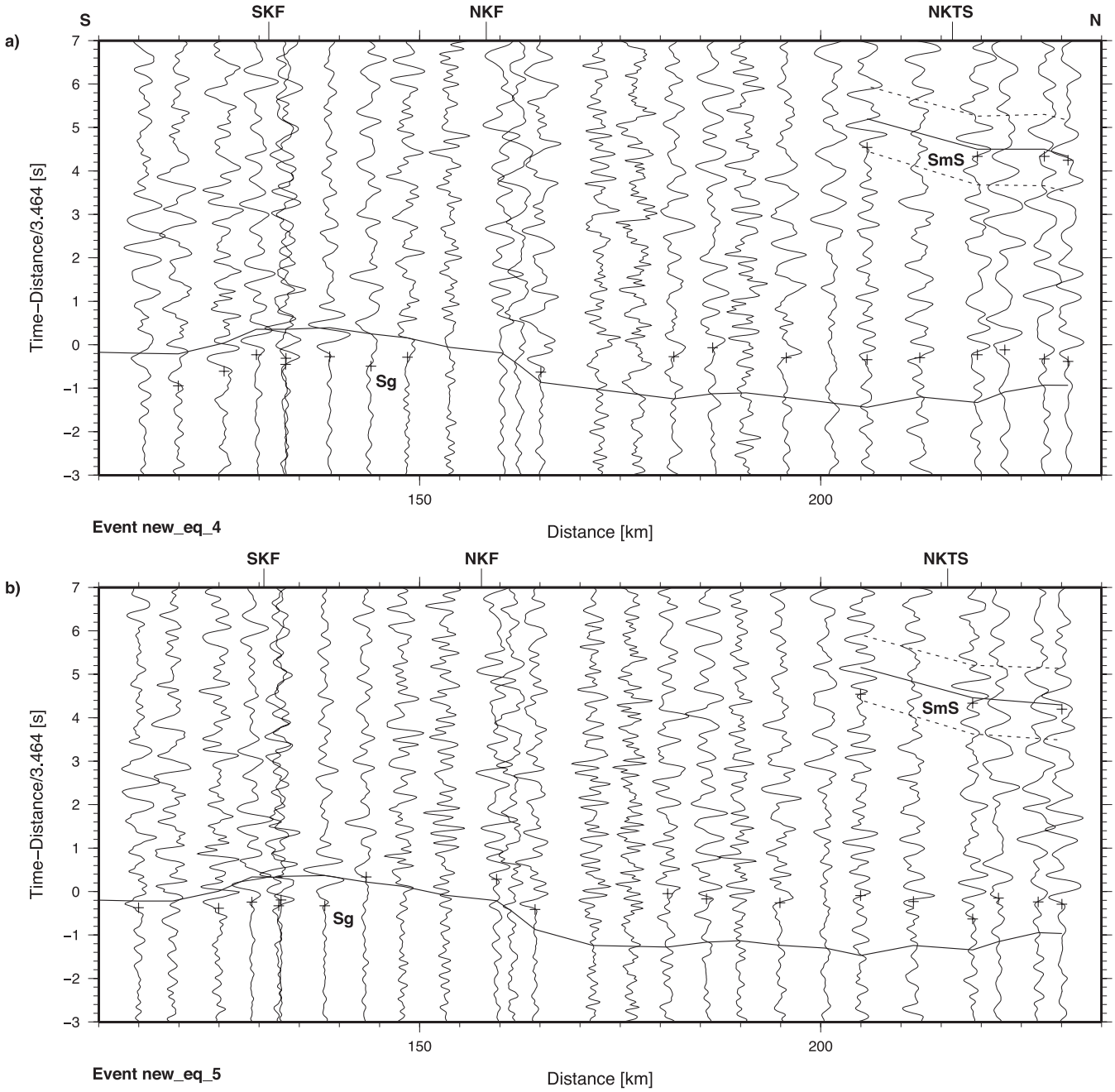

Figure 5. Seismic data from events (a) new_eq_4 and (b) new_eq_5 recorded along the middle part of the INDEPTH IV profile. The record sections show the N–S horizontal (approximately radial) component of *S*-wave motion reduced with a velocity of 3.46 km s^{-1}. Each trace is normalized individually and bandpass filtered from 0.1–5 Hz for new_eq_4 and 0.5–5 Hz for new_eq_5. Lines represent phases calculated from the model in Fig. 9, whereas crosses represent observed traveltimes. Dashed lines subparallel to the solid line for the *SmS* phase indicate traveltimes if the average Poisson's ratio for the region between 6–9 km depth b.s.l. and the Moho (Fig. 9) is changed from 0.24 to either 0.23 (earlier line) or 0.25 (later line). Key: see Figs 1, 3 and 4.

was derived. The two 1-D models were then combined to provide an initial 2-D model for the tomographic inversion (Fig. 6a). The profile orientation for this inversion was N7°E. After eight iterations the rms traveltime residual between the observed and theoretical traveltimes had decreased from 0.57 s ($\chi^2 = 16.17$) to 0.16 s ($\chi^2 = 0.88$), with little further improvement occurring. The χ^2 value of 0.88 and the fact that the rms traveltime residual for the final model (0.16 s) is close to the average standard deviation (0.18 s) of the picked traveltime data indicate that the data are adequately but not overfitted. The final model (Fig. 6b) has ray coverage down to about 10 km depth [5 km below sea level (b.s.l.)] as shown by the ray diagram (Fig. 6c), except in the central part of the Qaidam basin. However, a resolution test (Fig. 7) shows that checkerboard anomalies which are twice the size of the velocity node spacing (Fig. 7a) are only resolvable beneath the central part of the profile and in the vicinity of the shotpoint KS5 at the northern end of the profile down to about sea level (Fig. 7b).

In the tomogram (Fig. 6b) the lower velocities associated with the predominantly Neogene-Quaternary sediments of the Qaidam basin and the higher velocities associated with the predominantly

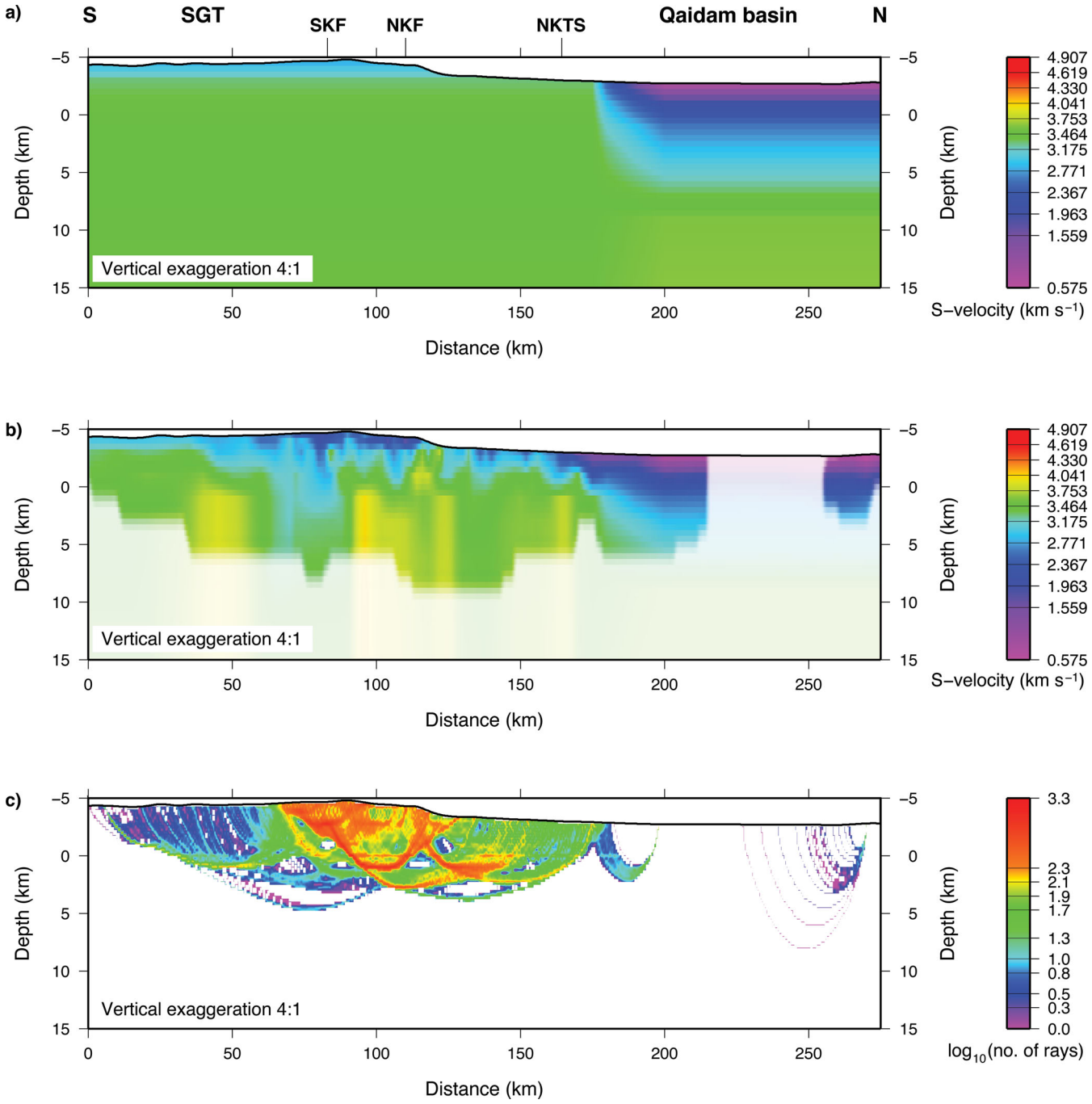

Figure 6. Upper crustal tomography using 14595 *Sg* arrivals and a N7°E orientation of the profile. (a) initial model, (b) final model, (c) ray diagram. In (b), brighter regions in the model have good ray coverage and are well resolved whereas fainter regions in the model have poor ray coverage and are poorly resolved. Key: see Fig. 1 and SGT, Songpan-Ganzi terrane.

Palaeozoic and Mesozoic upper crustal sequences of the northern Tibet plateau can be seen. There is also no evidence from this study that the Kunlun mountains are involved in large-scale northward thrusting over the Qaidam basin along a shallow-dipping thrust plane. In the vicinity and mainly to the south of the NKF and SKF lower velocities extend to greater depths and, in addition, a high velocity body beneath the Kunlun mountains just north of the NKF can be recognized. All three anomalies have already been recognized in the *P* velocity tomogram of Karplus *et al.* (2011), who interpreted the high velocity body to be because of one of the Palaeozoic/Mesozoic igneous (mainly granitic) intrusions that are quite frequently exposed at the surface along strike, in this part of the profile (Fig. 2). With respect to the low velocity anomalies, Karplus *et al.* (2011) noted that the maximum reduction in *P* velocity of 15 per cent near the NKF along the INDEPTH IV profile, is within the range of 7–20 per cent found by Wang *et al.* (2009) within the NKF zone to a depth of at least 1–2 km. In fact, Wang *et al.* (2009) found an even larger reduction of 30–45 per cent in *S* velocities. The maximum reduction in *S* velocity near either the NKF or SKF along the INDEPTH IV profile is about 33 per cent. Thus the low *S* velocity anomalies near the NKF and SKF along the INDEPTH IV profile are probably at least partly because of weakened, damaged

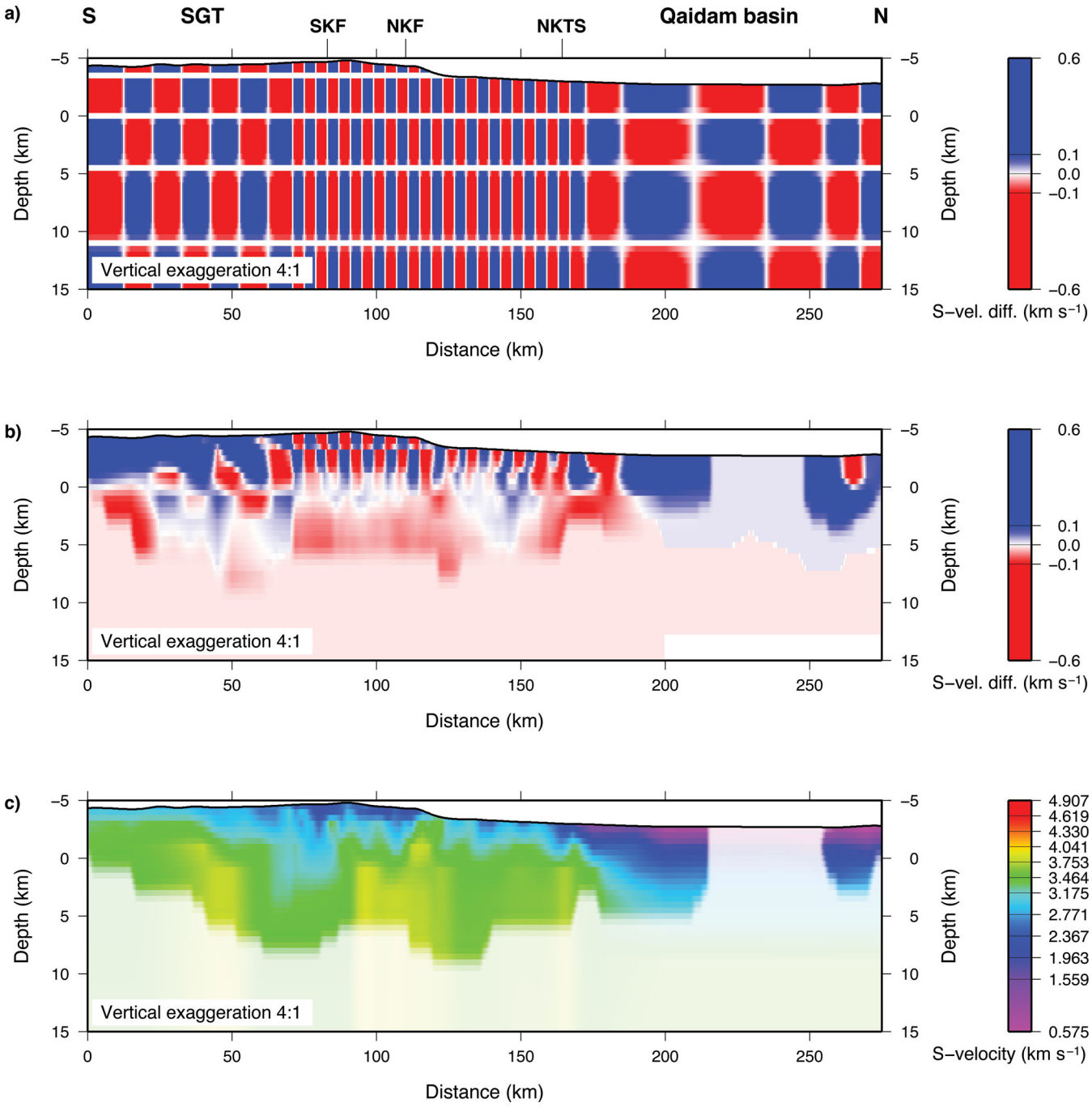

Figure 7. Resolution test using checkerboard anomalies. (a) original checkerboard anomalies, (b) retrieved checkerboard anomalies. (c) Model recovery test, for which the input traveltime data for the inversion were derived by ray tracing through the model shown in Fig. 6b. In (b) and (c), brighter regions in the models have good ray coverage and are well resolved whereas fainter regions in the models have poor ray coverage and are poorly resolved. Key: see Figs 1 and 6.

rocks associated with the fault zones. They could also be at least partly the result of the Quaternary sedimentary (alluvium, moraine, etc.) basins in the valleys mainly on the south sides of both of these faults (Fig. 2). Based on the resolution test discussed above, the low velocity anomalies mainly on the south sides of the NKF and SKF and the high velocity body just north of the NKF should be resolvable features. Further a model recovery test (Fig. 7c), in which the model to be recovered was the final model (Fig. 6b), shows that the low velocity anomalies mainly on the south sides of the NKF and SKF and the high velocity body just north of the NKF look very similar in the retrieved and final models.

The final tomogram (Fig. 6b) was derived for the average orientation (N7°E) of the whole profile. However, because of the rather crooked profile orientation especially in the central part of the profile between shots KS2 and KS4 and to check that profile orientation was not influencing the inversion, a tomogram was separately derived for a N–S profile orientation (Fig. 8a). This was accomplished by projecting the shot/receiver locations onto a N–S line before

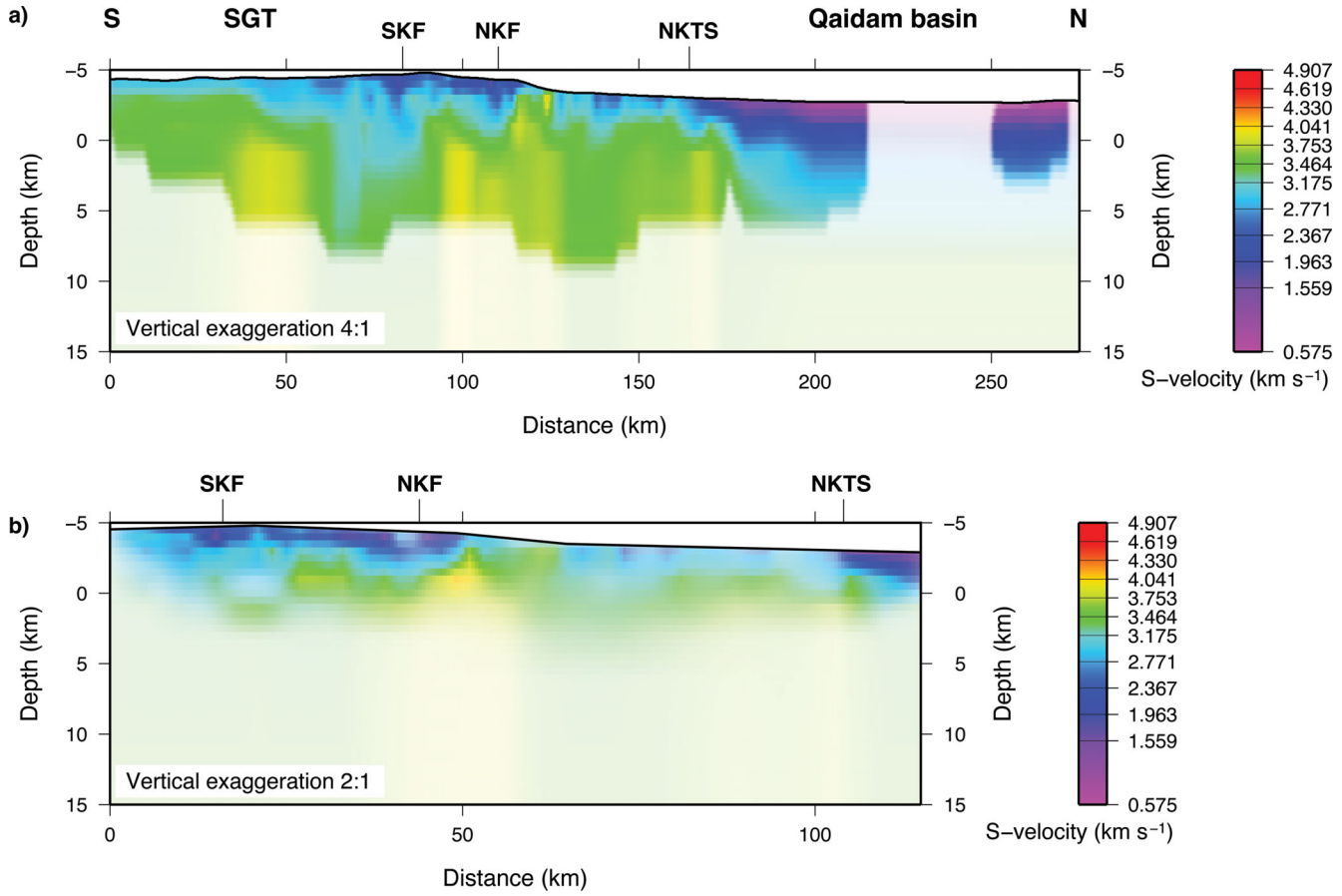

Figure 8. (a) Upper crustal tomography using 14595 *Sg* arrivals and a N–S orientation of the profile. (b) Upper crustal tomography using 13778 *Sg* arrivals and 3-D ray tracing. Brighter regions in the models have good ray coverage and are well resolved whereas fainter regions in the models have poor ray coverage and are poorly resolved. Note the change in distance scale between (a) and (b). Key: see Figs 1 and 6.

running the inversion. Also in this tomogram the low velocity anomalies mainly on the south sides of the NKF and SKF and the high velocity body north of the NKF can be recognized, although the high velocity body north of the NKF has a smaller lateral extent compared to the tomogram of the final model (Fig. 6b). In this tomogram (Fig. 8a) there is also some indication for a small high velocity body about 5 km to the north and closer to the surface. However, a model recovery test similar to that for the final model (Fig. 7c), shows that whereas the deeper high velocity body north of the NKF can be recovered, the small high velocity body about 5 km to the north and closer to the surface cannot be recovered. Finally, the data for the central part of the profile where the shot spacing was 1 km were inverted using 3-D ray tracing between the sources and receivers for the forward part of the problem, although only 2-D for the inverse part of the problem. In the resultant tomogram (Fig. 8b), the low velocity anomalies mainly on the south sides of the NKF and SKF can be recognized, albeit with poor resolution south of the SKF. Only one high velocity body just north of the NKF can be recognized as in the case of the final model (Fig. 6b). There is no indication for the smaller, shallower high velocity body as in the case of the tomogram derived from the N–S profile orientation (Fig. 8a).

Whole crust

The initial whole-crustal *S* velocity model incorporated the tomographic model derived by inverting 14595 *Sg* arrival times, down to 6–9 km depth b.s.l. (Fig. 6b). At depths greater than 6 km b.s.l., beneath the Songpan-Ganzi terrane and Kunlun mountains and 9 km b.s.l. under the Qaidam basin, initial *S* velocities were derived by dividing the velocities of the *P* velocity model (Fig. 8c in Karplus *et al.* 2011) by 1.732 (square root of 3), resulting in a Poisson's ratio (σ) of 0.25 for this part of the initial model. In addition, the layer boundaries from the *P* velocity model were incorporated into the initial *S* velocity model and were held fixed during the *S* velocity modelling. Using the same ray tracing and inversion techniques described above, but with only two unknown model parameters, only one iteration, in which the rms traveltime residual between the 21 observed and theoretical *SmS* phase traveltimes decreased from 0.82 s ($\chi^2 = 17.44$) to 0.27 s ($\chi^2 = 1.98$), was required to derive a final model (Fig. 9a), which is significantly different from the initial model at the 99.98 per cent confidence level. With respect to the initial model, in the final model the *S* velocity between 6 km depth b.s.l. and the Moho beneath the Songpan-Ganzi terrane and Kunlun mountains increased by 0.06 km s^{-1} resulting in a σ of 0.24 and the *S* velocity between 9 km depth b.s.l. and the Moho below the Qaidam basin increased by 0.01 km s^{-1} resulting in a σ of 0.25 (Fig. 9b). As a comparison between the rays for the *SmS* and *PmP* phases shows (Fig. 10), very similar regions beneath the profile are covered by both families of rays. Thus it is justified to calculate the average σ for the regions between 6–9 km depth b.s.l. and the Moho. As the number of rays is small (Fig. 10) and no further intracrustal *S* reflections could be identified in the data, further refinement of the *S* velocity and Poisson's ratio models for the crust below

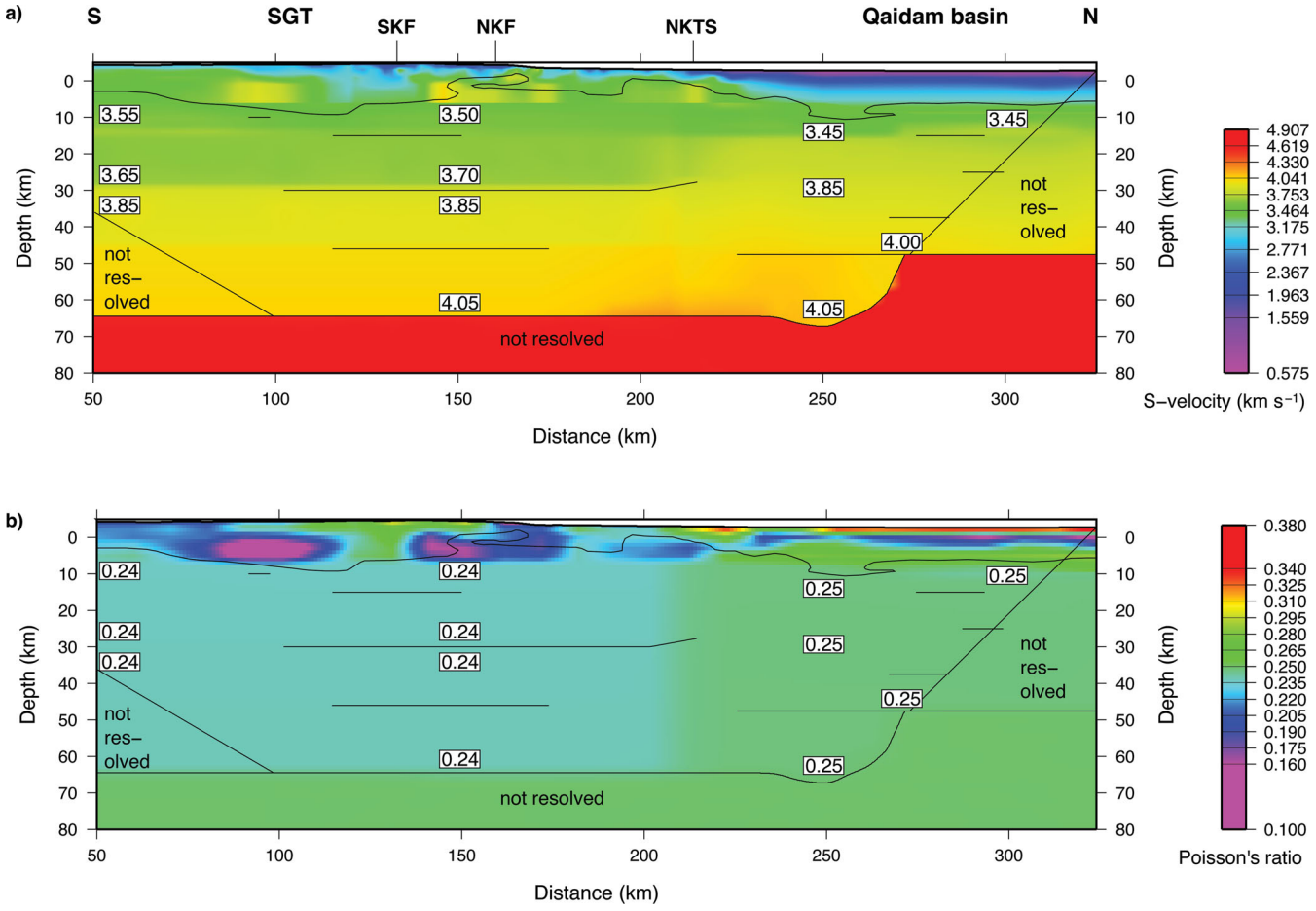

Figure 9. (a) *S* velocity model and (b) smoothed Poisson's ratio model along the INDEPTH IV profile. In (b), smoothing is 10 km in the horizontal direction and 2.5 km in the vertical direction. Uppermost boundary represents the 5.9 km s^{-1} *P* velocity contour as defined by Karplus *et al.* (2011). This boundary represents the base of the Songpan-Ganzi flysch south of the NKTS and the base of the Mesozoic and/or Palaeozoic sediments north of the NKTS. Velocities in km s^{-1}. Key: see Figs 1 and 6.

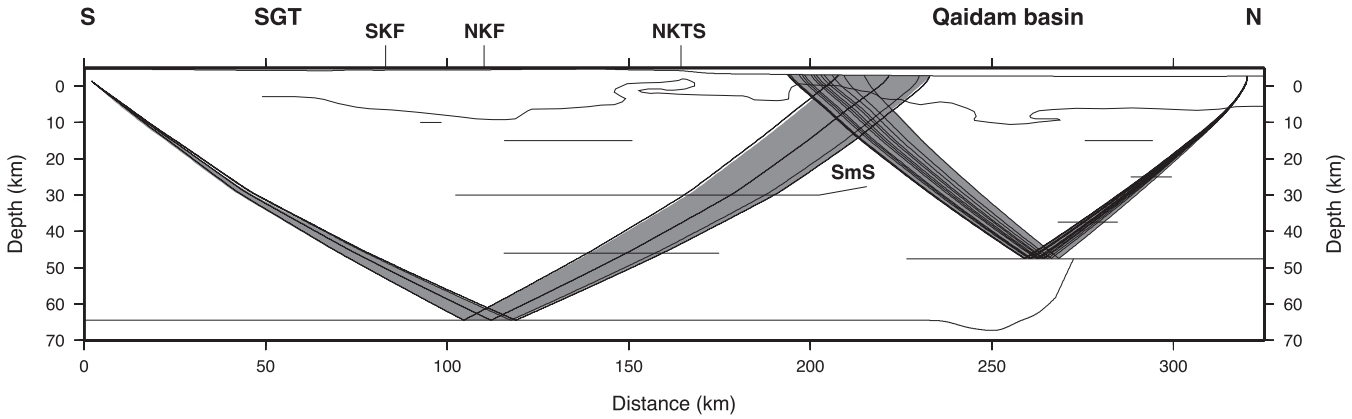

Figure 10. Ray diagram for the final iteration of the *SmS* phase. The shaded areas represent the regions traversed by the *PmP* phase (see also Karplus *et al.* 2011), for the same source–receiver configurations as those for the *SmS* phase. Key: see Figs 1 and 6.

6–9 km depth b.s.l. is not really justified. Further, the χ^2 value of 1.98 and the fact that the rms traveltime residual for the final model (0.27 s) is close to the average standard deviation (0.20 s) of the picked traveltime data again indicate that the data are adequately but not overfitted. In considering the accuracy of the average σ for the regions between 6–9 km depth b.s.l. and the Moho, it can be noted that to obtain an accuracy of ± 0.01 in σ requires an accuracy in the average *P* and *S* velocities of about 1 per cent (Christensen 1996). If one varies the average *P* velocity by 1 per cent then this causes a traveltime difference for the *PmP* phase of about 0.21 s beneath the

Qaidam basin and about 0.36 s beneath the Songpan-Ganzi terrane and Kunlun mountains. Similarly, if one varies the average *S* velocity by 1 per cent then this causes a traveltime difference for the *SmS* phase of about 0.34 s beneath the Qaidam basin and about 0.60 s beneath the Songpan-Ganzi terrane and Kunlun mountains. In all cases this traveltime difference is greater than the average standard deviation of the picked traveltime data. In the record sections (Figs 4 and 5), the solid lines indicate *SmS* traveltimes from the final model whereas sub-parallel dashed lines indicate traveltimes if the average σ for the region between 6–9 km depth b.s.l. and the Moho (Fig. 9) are changed from 0.24 to either 0.23 or 0.25 in the Songpan-Ganzi terrane and Kunlun mountains or from 0.25 to either 0.24 or 0.26 in the Qaidam basin. Despite the uncertainty in picking the precise onset of the *SmS* phase (Figs 4 and 5), it is clear that changes in σ greater than ± 0.01 are only possible if the *SmS* phase has been misidentified.

As the *P* velocity tomogram for the upper part of the crust has better resolution (see Figs 8b, 9a and B1b in Karplus *et al.* 2011) than the corresponding *S* velocity tomogram (Figs 6b–c and 7b), then the resulting Poisson's ratio model (Fig. 9b) for the upper part of the crust can only be expected to be reliable in the regions where the *S* velocity tomogram is well resolved. All major features described below from the Poisson's ratio model for the upper crust reside in those regions where the *S* velocity model for the upper crust is well resolved. Poisson's ratio (σ) in the region of the upper crust resolved by both the *P* velocity tomogram of Karplus *et al.* (2011) and the tomogram derived from the *Sg* phase data in this study, varies from 0.10–0.38 (Fig. 9b). Beneath the Songpan-Ganzi terrane and Kunlun mountains high values in excess of 0.30 only exist very close to the surface near the SKF and NKF. As noted above Wang *et al.* (2009) found large reductions in *P* and *S* velocities within the NKF zone. As a result of these reduced velocities Wang *et al.* (2009) also derived σ in excess of 0.30 within the NKF zone. Thus the most likely cause of the high σ near the NKF and SKF along the INDEPTH IV profile would seem to be weakened, damaged rocks associated with the fault zones. Between 1–6 km depth b.s.l., the Songpan-Ganzi terrane and Kunlun mountains are dominated by low σ values. South of the NKF the regions of low σ occur predominantly within the Songpan-Ganzi flysch, the base of which was defined by Karplus *et al.* (2011) to be the 5.9 km s^{-1} *P* velocity contour, which is the uppermost boundary shown in the *S* velocity and Poisson's ratio models (Figs 9a–b). This would suggest that the lower parts of the Songpan-Ganzi flysch complex are rich in quartz. The Triassic rocks of the Songpan-Ganzi flysch are also exposed at the surface along the profile for about 20 km north of the NKF. Thus some of the near-surface low σ in this area probably correlate with quartz-rich rocks of the Songpan-Ganzi flysch. At greater depths in this area low σ probably correlate with granitic intrusions rich in quartz. As noted above, such intrusions are exposed at the surface along strike, in this part of the profile (Fig. 2). The high velocity body just north of the NKF already described and interpreted as an intrusion above, could alternatively be, because of its high *P* and *S* velocities and low σ, metamorphic rocks (gneiss, metapelite or granulite), perhaps tectonically emplaced at higher levels than those at which the rocks originated. This fact is deduced from a comparison between the derived *P* and *S* velocities along the seismic profile and a data bank of measured *P* and *S* velocities for 416 rocks of many different types (Stadtlander *et al.* 1999 and references therein) at appropriate pressure and temperature. Further north, where the predominantly granodioritic rocks of the North Kunlun batholith are exposed at the surface, the low σ especially at greater depths are most probably associated with quartz-rich variants of these rocks. North of the NKTS the 5.9 km s^{-1} *P* velocity contour probably correlates with the boundary between the Mesozoic and/or Palaeozoic sediments and the crystalline basement beneath the Qaidam basin. As in the Songpan-Ganzi terrane and Kunlun mountains, high values of σ in excess of 0.30 only exist close to the surface, possibly indicating locally clay-rich sediments (Kenter *et al.* 2007). At 3–5 km depth a band of low σ probably indicates sediments rich in quartz whereas the remaining 3 km down to the 5.9 km s^{-1} *P* velocity contour has normal σ of around 0.25.

DISCUSSION

Average crustal *P* velocity ranges from 6.3–6.4 km s^{-1} beneath the Songpan-Ganzi terrane and Kunlun mountains and from 5.85–5.95 km s^{-1} under the Qaidam basin (see also Karplus *et al.* 2011). Excluding the Cenozoic sediments results in an average *P* velocity between 1 km depth b.s.l. and the Moho of 6.3–6.4 km s^{-1} below the Qaidam basin (see also Karplus *et al.* 2011). Average crustal *S* velocity ranges from 3.7–3.8 km s^{-1} beneath the Songpan-Ganzi terrane and Kunlun mountains and from 3.3–3.4 km s^{-1} under the Qaidam basin. Again, excluding the Cenozoic sediments results in an average *S* velocity between 1 km depth b.s.l. and the Moho of 3.65–3.7 km s^{-1} below the Qaidam basin. These values compare with the global average, which also excludes low velocity sediments, for continental crust of 3.65 km s^{-1} (Christensen 1996). This then results in average crustal σ of 0.23–0.24 beneath the Songpan-Ganzi terrane and Kunlun mountains and 0.255–0.27 below the Qaidam basin. Beneath the Songpan-Ganzi terrane and Kunlun mountains the average σ between about 6 km depth b.s.l. and the Moho at about 65 km depth b.s.l. is 0.24. Under the Qaidam basin the average σ between about 9 km depth b.s.l. and the Moho at about 48 km depth b.s.l. is 0.25. Although the average crustal σ beneath the Qaidam basin is close to the global average of 0.265–0.27 for continental crust (Zandt & Ammon 1995; Christensen 1996), the crust below the Cenozoic basin sediments between 1 km depth b.s.l. and the Moho only has an average σ of 0.245–0.25 which is less than the global average for continental crust. In this respect, it is interesting to note that the crust of the Qaidam basin below the Cenozoic sediments has an average σ, which is less than the Tarim and Sichuan basins, which are thought to be underlain by strong crust which impedes the Indo-Asian collision. For example, the Tarim basin has an average σ of 0.26 for the crust below the sediments (Wang *et al.* 2003), whereas the Sichuan basin has an average crustal σ of 0.27 (Wang *et al.* 2010). Although the Qaidam crust may have lost some of its lower mafic part in a previous orogeny, it seems unlikely that any of the Qaidam crust has already been lost because of delamination following eclogitization in the present Himalayan orogenic cycle. The reason for this is that the region of the Qaidam basin has been a basin since the Palaeocene–Early Eocene (Yin *et al.* 2008) which is more or less all through the period of the present Himalayan orogenic cycle, and the present crustal thickness is only about 50 km (Karplus *et al.* 2011). Yin *et al.* (2008) envisage an initial crustal thickness at the start of the Cenozoic era of greater than about 32 km. Thus it would seem that a somewhat more felsic crust than average beneath the Qaidam basin is presently being involved in the collision at the NE margin of Tibet. This somewhat more felsic than average crust is then weaker and more easily deformable (see e.g. Chen *et al.* 2006; Bürgmann & Dresen 2008) and thus may facilitate the collision and promote the formation of new high plateau crust at the NE margin of Tibet. In this respect it should be noted that the crust of the Songpan-Ganzi terrane and Kunlun

mountains, south of the Qaidam basin, has an even lower average crustal σ of 0.23–0.24 and is thus presumably even weaker and more easily deformable than the crust beneath the Qaidam basin. This would then be additional evidence to support the hypothesis of Karplus *et al.* (2011) that 'the high Tibetan Plateau may be thickening northward into south Qaidam as its weak, thickened lower crust is injected beneath stronger Qaidam crust'.

The low average crustal σ of 0.23–0.24 beneath the Songpan-Ganzi terrane and Kunlun mountains derived in this study is in agreement with other estimates from the northeastern part of the plateau. For example, using wide-angle data in NE Tibet about 300 km southeast of the INDEPTH IV profile, Galvé *et al.* (2006) derived an average crustal value for σ of 0.25 in the northern Qiangtang terrane just south of the Jinsha suture and Jiang *et al.* (2006) derived an even lower average crustal value for σ of 0.22 north of the Jinsha suture. From receiver functions in the vicinity of the INDEPTH IV profile, Vergne *et al.* (2002) and Yue *et al.* (2012) obtained an average crustal value for σ of 0.26 in the Songpan-Ganzi terrane, whereas Kind *et al.* (2002) derived a value of about 0.25. These average crustal values derived from receiver-function methods can show rapid lateral changes (e.g. Yue *et al.* 2012) perhaps in part because of poor stability of the methods, perhaps in part because of lateral changes in sedimentary cover affecting the whole-crustal estimates. Further, Galvé *et al.* (2006) derived a value for σ of 0.25 for the lower crust in the northern Qiangtang terrane just south of the Jinsha suture and Jiang *et al.* (2006) derived a value for σ of 0.20 for the lower crust north of the Jinsha suture (Fig. 11a). The value of 0.24 derived in this study for the crust between 6 km depth b.s.l. and the Moho lies between these values. In other parts of Tibet and the Pamir similar values for σ have been found for the lower crust, although in yet other areas higher values have been found (Fig. 11a). Included in these other areas, is an area in north-central Tibet (89.23°E, 34.40°N, Fig. 11a) about 500 km west of the southern end of the INDEPTH IV profile where metasedimentary and mafic xenoliths from lower crustal depths of 30–50 km were recovered. From the mineral assemblages in these xenoliths, *P* velocities of 6.1–7.2 km s^{-1} and σ of 0.258–0.272 were derived for the lower crust in this area (Hacker *et al.* 2000). All the values shown (Fig. 11a), except those of Jiang *et al.* (2006) and the lower value of Zhang & Klemperer (2005) for the east end of the profile they interpreted, lie within the range of values, 0.24–0.29, found by other studies globally (Holbrook *et al.* 1992). Jiang *et al.* (2006) invoked anisotropy as a possible explanation for the very low value for σ of 0.20 in the lower crust of the Songpan-Ganzi terrane, but still concluded that σ for the isotropic rock in this case would not exceed 0.25. In this respect, it is interesting to note that the profiles for which values for σ for the lower crust in NE Tibet have been derived vary in orientation from NW–SE (Galvé *et al.* 2006), through N–S in this study, assuming no significant variation in σ between 6 and 9 km depth b.s.l. and the Moho, to NE–SW (Jiang *et al.* 2006). The lower crust between 25 and 30 km depth b.s.l. and the Moho beneath the INDEPTH IV profile has *P* velocities varying from 6.6 km s^{-1} at the top to around 6.9 km s^{-1} at the base (Karplus *et al.* 2011). These *P* velocities together with a σ of 0.24 beneath the Songpan-Ganzi terrane and Kunlun mountains or 0.25 beneath the Qaidam basin, assuming an isotropic situation and no variation in σ between 6 and 9 km depth b.s.l. and the Moho imply, according to Holbrook *et al.* (1992), intermediate granulites in the upper part of the lower crust transitioning to granulite facies metapelites in the lower part (Fig. 11b).

In central Tibet, Mechie *et al.* (2004) used a comparison of *P*- and *S*-wave data to interpret as the $\alpha-\beta$ quartz transition (ABQT) an intracrustal boundary at 18–32 km depth, corresponding to isotherms of 700 °C and 800 °C respectively. Although variations in Poisson's ratio (σ) across this depth range on the INDEPTH IV profile cannot be sufficiently resolved to be definitive, our inability to recognize *S*-wave reflections, albeit on noisy data, corresponding to *P*-wave reflections at 10–15 km b.s.l. (Karplus *et al.* 2011) suggests these boundaries might correspond to the ABQT (Mechie *et al.* 2004). If the boundaries at 10–15 km depth b.s.l. in the southern portion of the profile are in fact associated with the ABQT, then this implies a temperature of 675–680 °C at 10 km b.s.l. where the boundary is at 10 km b.s.l. and a temperature of 710–715 °C at 15 km b.s.l. where the boundary is at that depth. As in central Tibet, high electrical conductivity beneath these depths (Unsworth *et al.* 2004; Le Pape *et al.* 2012) is consistent with the high-inferred temperatures. High temperatures and high electrical conductivities at mid-crustal depths lend support to models involving ductile flow in the deeper (middle and/or lower) crust beneath Tibet (see e.g. Zhao & Morgan 1987; Clark & Royden 2000; Klemperer 2006; Zhang *et al.* 2011). The low average σ of 0.24 for the crust between 6 km depth b.s.l. and the Moho in the southern portion of the profile under the Songpan-Ganzi terrane and Kunlun mountains raises the question of whether the quartz, if present, in the deeper crust is in the α or β state. In this respect, suffice it to be stated that if the temperature at 50 km depth is below 920 °C or at 60 km depth below 990°C, then quartz will be in the α state and will have a low σ.

CONCLUSIONS

Analysis of *S*-wave recordings from controlled sources and earthquakes along the INDEPTH IV profile across the Kunlun mountains in NE Tibet has led to the development of a tomographic model for the *S* velocity structure of the upper 10–15 km of the crust beneath the profile, and measurement of an average *S* velocity for the deeper crust. Combining this crustal *S* velocity model (Fig. 9a) with the previously derived crustal *P* velocity model (Karplus *et al.* 2011) yields a Poisson's ratio (σ) model (Fig. 9b) for the crust beneath the INDEPTH IV profile. The major features which can be recognized in the upper crustal *S* velocity tomogram are the lower velocities associated with the predominantly Neogene-Quaternary sediments of the Qaidam basin to the north and the higher velocities associated with the predominantly Palaeozoic and Mesozoic rocks of the Songpan-Ganzi terrane and Kunlun mountains to the south. Further, this study shows no evidence that the Kunlun mountains are involved in large-scale overriding of the Qaidam basin along a shallow south-dipping thrust. Two regions of low velocity in the vicinity and mainly to the south of the NKF and the SKF have been recognized, that are probably partly because of weakened, damaged rocks associated with the fault zones and partly because of the Quaternary sedimentary basins occurring in the valleys mainly on the south sides of both of these faults. A high velocity body at 2–4 km depth beneath the Kunlun mountains just north of the NKF may be due either to an igneous intrusion or metamorphic rocks perhaps tectonically emplaced at higher structural levels than they originated.

Below the upper 10–15 km of the crust, the remainder of the crust down to the Moho has an average σ of 0.24 beneath the Songpan-Ganzi terrane and Kunlun mountains and 0.25 below the Qaidam basin. Assuming an isotropic situation and no significant variation in σ between 10–15 km depth and the Moho, then the lower crust between 25–30 km depth b.s.l. and the Moho with *P* velocities varying from 6.6 km s^{-1} at the top to around

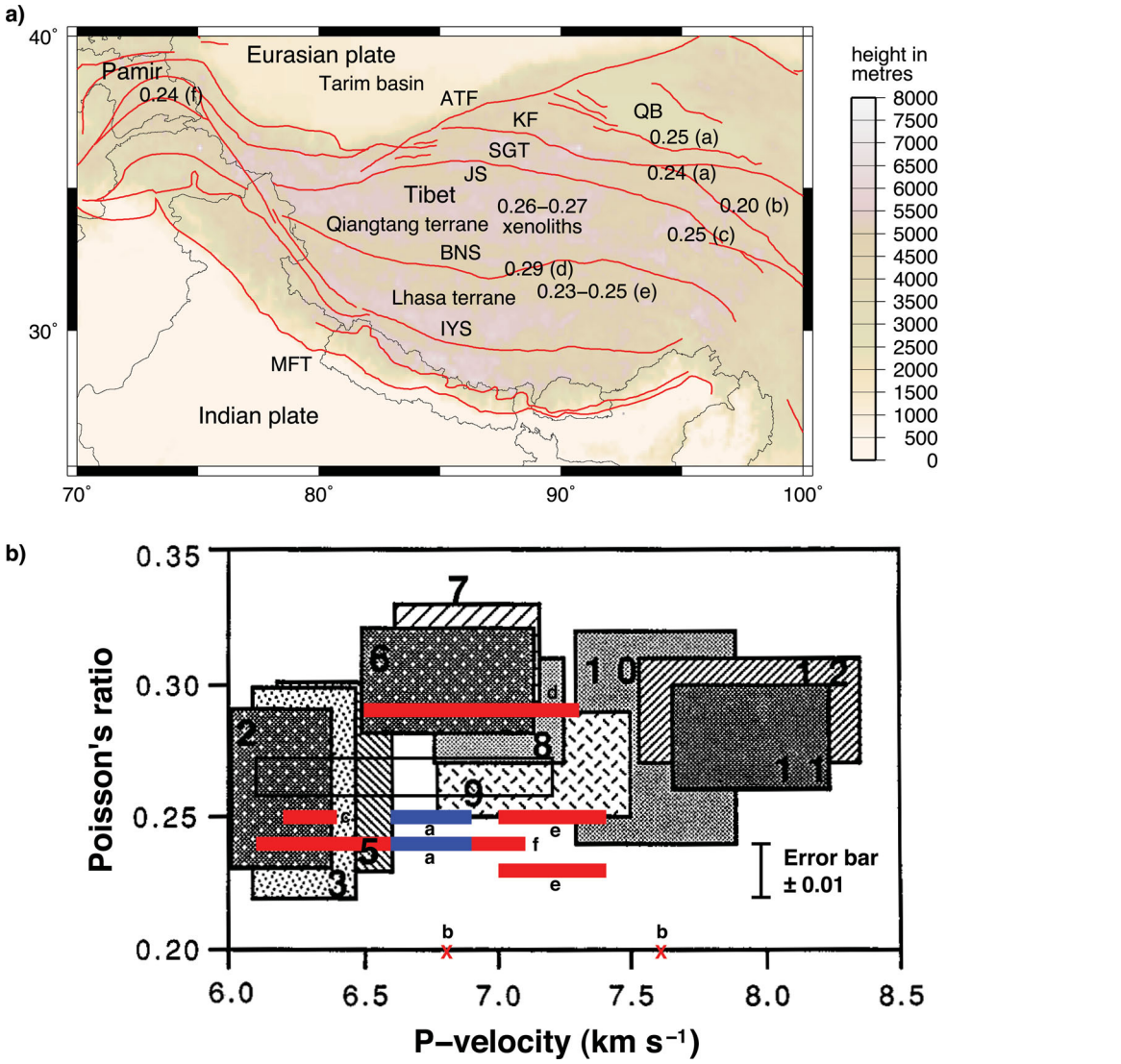

Figure 11. (a) Map showing location of wide-angle lower crustal Poisson's ratio (σ) measurements in Tibet and the Pamir. (b) Comparison between lower crustal velocities and σ measured along various seismic profiles in Tibet and the Pamir, velocities and σ calculated from lower crustal xenoliths from Tibet (Hacker *et al.* 2000) and velocities and σ measured on possible lower crustal rock types in the laboratory (after Holbrook *et al.* 1992). The measurements from wide-angle seismic profiles [letter after σ value in (a) and blue bars, this study and red bars, previous studies in (b)] are (a) INDEPTH IV profile, this study, (b) profile in Songpan-Ganzi terrane about 300 km to the southeast of INDEPTH IV (Jiang *et al.* 2006), (c) profile in Qiangtang terrane about 300 km to the southeast of INDEPTH IV (Galvé *et al.* 2006), (d) INDEPTH III profile in Lhasa and Qiangtang terranes (Zhao *et al.* 2001; Mechie *et al.* 2004), (e) profile in Lhasa terrane (Zhang & Klemperer 2005) and (f) profile in the Pamir (Mechie *et al.* 2012). The upper blue bar shows the situation beneath the Qaidam basin and the lower blue bar the situation beneath the Songpan-Ganzi terrane and Kunlun mountains. An appropriate error bar of ±0.01 for σ is shown (see also discussion in text). The open black box in (b) represents the field covered by the xenoliths found about 500 km west of the southern end of the INDEPTH IV profile (Hacker *et al.* 2000). The fields with patterns represent felsic amphibolite gneiss (2), quartz-mica schist & felsic granulite (3), intermediate granulite (5), anorthosite (6), mafic granulite (7), amphibolite (8), granulite facies metapelite (9), pyroxenite (10), eclogite (11) and peridotite/dunite (12). Key: for JS, BNS and SGT, see Figs 1 and 6; ATF, Altyn Tagh Fault; KF, Kunlun Fault; QB, Qaidam basin; IYS, Indus-Yarlung Suture; MFT, Main Frontal Thrust.

6.9 km s^{-1} at the base (Karplus *et al.* 2011) and σ of 0.24 beneath the Songpan-Ganzi terrane and Kunlun mountains or 0.25 beneath the Qaidam basin should comprise, according to Holbrook *et al.* (1992), intermediate granulites in the upper part transitioning to granulite facies metapelites in the lower part (Fig. 11b). As the pre-Cenozoic Qaidam crust only has a σ of 0.245–0.25, then it appears that the pre-Cenozoic Qaidam crust involved in the collision is more felsic and thus weaker and more easily deformable than normal continental crust with a global average σ of 0.265–0.27 (Zandt & Ammon 1995; Christensen 1996). This feature then probably facilitates the collision and promotes the formation of new high plateau crust at the NE margin of Tibet. In this respect it should be noted that, south of the Qaidam basin, the crust of the Songpan-Ganzi terrane and Kunlun mountains has an even lower average crustal σ of 0.23–0.24 and is thus presumably even weaker and more easily deformable than the crust beneath the Qaidam basin. This would then support the hypothesis of Karplus *et al.* (2011) that 'the high Tibetan Plateau may be thickening northward into south Qaidam as its weak, thickened lower crust is injected beneath stronger Qaidam crust'.

ACKNOWLEDGMENTS

The INDEPTH IV project was funded by the Deutsche Forschungsgemeinschaft, the Deutsches GeoForschungsZentrum—GFZ, NSF-EAR-CD-0409939 and CGS-1212010511809 in China. The instruments used in the field program were provided by the Geophysical Instrument Pool of the Deutsches GeoForschungsZentrum—GFZ, the NERC geophysical equipment pool, Seis-UK node (University of Leicester, www.le.ac.uk/seis-uk) and the PASSCAL facility of the Incorporated Research Institutions for Seismology (IRIS) through the PASSCAL Instrument Center at New Mexico Tech. Data collected during this experiment with the PASSCAL instruments are available through the IRIS Data Management Center. The facilities of the IRIS Consortium are supported by the National Science Foundation under Cooperative Agreement EAR-0004370 and by the Department of Energy National Nuclear Security Administration. The 6th Geophysical Brigade is thanked for contracting to drill and execute the shots and provide a 1000-channel Sercel recording unit. The INDEPTH field team is thanked for deploying the seismic instruments and overseeing the drilling and blasting operations. The help of the vehicle drivers is also acknowledged. M. Paschke helped with the data processing and model calculations. All of the figures were prepared with the help of the GMT plotting routines (Wessel & Smith 1991).

REFERENCES

Bally, A.W. *et al*., 1986. Notes on sedimentary basins in China–report of the American Sedimentary Basins Delegation to the People's Republic of China. Open-File Rep, *U.S. Geol. Surv.*, **108,** 86–327.

Bürgmann, R. & Dresen, G., 2008. Rheology of the lower crust and upper mantle: evidence from rock mechanics, geodesy, and field observations, *Annu. Rev. Earth planet. Sci.,* **36,** 531–567, doi:10.1146/annurev.earth.36.031207.124326.

Burchfiel, B., Deng, Q., Molnar, P., Royden, L., Wang, Y., Zhang, P. & Zhang, W., 1989. Intracrustal detachment within zones of continental deformation, *Geology,* **17,** 748–752.

Chen, S., Hiraga, T. & Kohlstedt, D.L., 2006. Water weakening of clinopyroxene in the dislocation creep regime, *J. geophys. Res.,* **111,** B08203, doi:10.1029/2005JB003885.

Christensen, N.I., 1996. Poisson's ratio and crustal seismology, *J. geophys. Res.,* **101,** 3139–3156.

Clark, M.K. & Royden, L.H., 2000. Topographic ooze; building the eastern margin of Tibet by lower crustal flow, *Geology,* **28,** 703–706.

Galvé, A., Jiang, M., Hirn, A., Sapin, M., Laigle, M., de Voogd, B., Gallart, J. & Qian, H., 2006. Explosion seismic P and S velocity and attenuation constraints on the lower crust of the North–Central Tibetan Plateau, and comparison with the Tethyan Himalayas: implications on composition, mineralogy, temperature, and tectonic evolution, *Tectonophysics,* **412,** 141–157, doi:10.1016/j.tecto.2005.09.010.

Hacker, B.R., Gnos, E., Ratschbacher, L., Grove, M., McWilliams, M., Sobolev, S.V., Wan, J. & Zhenhan, W., 2000. Hot and dry deep crustal xenoliths from Tibet, *Science,* **287,** 2463–2466.

Holbrook, W.S., Mooney, W.D. & Christensen, N.I., 1992. The seismic velocity structure of the deep continental crust, in *Continental Lower Crust, Developments in Geotectonics,* Vol. 24, pp. 1–43, eds Fountain, D.M., Arculus, R. & Kay, R.W., Elsevier, Amsterdam.

Jiang, M. *et al*., 2006. Crustal thickening and variations in architecture from the Qaidam basin to the Qang Tang (North – Central Tibetan Plateau) from wide-angle reflection seismology, *Tectonophysics,* **412,** 121–140, doi:10.1016/j.tecto.2005.09.011.

Karplus, M.S., Zhao, W., Klemperer, S.L., Wu, Z., Mechie, J., Shi, D., Brown, L.D. & Chen, C., 2011. Injection of Tibetan crust beneath the south Qaidam Basin: evidence from INDEPTH IV wide-angle seismic data, *J. geophys. Res.,* **116,** B07301, doi:10.1029/2010JB007911.

Kenter, J.A.M., Braaksma, H., Verwer, K. & van Lanen, X.M.T., 2007. Acoustic behavior of sedimentary rocks: geologic properties versus Poisson's ratios, *Leading Edge,* **26,** 436–444.

Kidd, W.S.F. *et al*., 1988. Geological mapping of the Chinese-British Tibetan (Xizang-Qinghai) plateau geotraverse route, *Phil. Trans. R. Soc. Lond., A.,* **327,** 287–305.

Kind, R. *et al*., 2002. Seismic images of crust and upper mantle beneath Tibet: evidence for Eurasian plate subduction, *Science,* **298,** 1219–1221.

Klemperer, S.L., 2006. Crustal flow in Tibet: geophysical evidence for the physical state of Tibetan lithosphere, and inferred patterns of crustal flow, in *Channel Flow, Ductile Extrusion and Exhumation in Continental Collision Zones,* Geol. Soc. Lond. Spec. Publ. Vol. 268, pp. 39–70, eds Law, R.D., Searle, M.P. & Godin, L., Geological Society, London, doi:10.1144/GSL.SP.2006.268.01.03.

Le Pape, F., Jones, A.G., Vozar, J. & Wenbo, W., 2012. Penetration of crustal melt beyond the Kunlun Fault into northern Tibet, *Nat. Geosci.,* **5,** 330–335, doi:10.1038/ngeo1449.

Lee, W.H.K. & Valdés, C.M., 1985. HYPO71PC: a personal computer version of the HYPO71 earthquake location program. Open-File Rep, U.S. Geol. Surv., 85–749, 43pp.

Lutter, W.J., Nowack, R.L. & Braile, L.W., 1990. Seismic imaging of upper crustal structure using travel times from the PASSCAL Ouachita experiment, *J. geophys. Res.,* **95,** 4621–4631.

Mechie, J. *et al*., 2004. Precise temperature estimation in the Tibetan crust fom seismic detection of the α-β quartz transition, *Geology,* **32,** 601–604, doi:10.1130/G20367.1.

Mechie, J. *et al*., 2012. Crustal and uppermost mantle velocity structure along a profile across the Pamir and southern Tien Shan as derived from project TIPAGE wide-angle seismic data, *Geophys. J. Int.,* **188,** 385–407, doi:10.1111/j.1365-246X.2011.05278.x.

Mock, C., Cantagrel, J. & Arnaud, N.O., 1999. An early unroofing in northeastern Tibet? Constraints from $^{40}Ar/^{39}Ar$ thermochronology on granitoids from the eastern Kunlun range (Qinghai, NW China), *Earth planet. Sci. Lett.,* **171,** 107–122.

Molnar, P., Burchfiel, B.C., Ziyun, Z., K'uangyi, L., Shuji, W. & Minmin, H., 1987. Geologic evolution of northern Tibet: results of an expedition to Ulugh Muztagh, *Science,* **235,** 299–305.

Podvin, P. & Lecomte, I., 1991. Finite difference computation of traveltimes in very contrasted velocity models: a massively parallel approach and its associated tools, *Geophys. J. Int.,* **105,** 271–284.

Schneider, W.A., Ranzinger, K.A., Balch, A.H. & Kruse, C., 1992. A dynamic programming approach to first arrival traveltime computation in media with arbitrarily distributed velocities, *Geophysics,* **57,** 39–50.

Stadtlander, R., Mechie, J. & Schulze, A., 1999. Deep structure of the southern Ural mountains as derived from wide-angle seismic data, *Geophys. J. Int.,* **137,** 501–515.

Unsworth, M. *et al*., 2004. Crustal and upper mantle structure of northern Tibet imaged with magnetotelluric data, *J. geophys. Res.,* **109,** B02403, doi:10.1029/2002JB002305.

Vergne, J., Wittlinger, G., Hui, Q., Tapponnier, P., Poupinet, G., Mei, J., Herquel, G. & Paul, A., 2002. Seismic evidence for stepwise thickening of the crust across the NE Tibetan plateau, *Earth planet. Sci. Lett.,* **203,** 25–33.

Vidale, J., 1988. Finite-difference calculation of travel times, *Bull. seism. Soc. Am.,* **78,** 2062–2076.

Wang, C.-Y., Mooney, W.D., Ding, Z., Yang, J., Yao, Z. & Lou, H., 2009. Shallow seismic structure of Kunlun fault zone in northern Tibetan Plateau, China: implications for the 2001 M_S8.1 Kunlun earthquake, *Geophys. J. Int.,* **177,** 978–1000, doi:10.1111/j.1365-246X.2009.04049.x.

Wang, C.-Y., Zhu, L., Lou, H., Huang, B.-S., Yao, Z. & Lou, X., 2010. Crustal thicknesses and Poisson's ratios in the eastern Tibetan plateau and their tectonic implications, *J. geophys. Res.,* **115,** B11301, doi:10.1029/2010JB007527.

Wang, Y., Mooney, W.D., Yuan, X. & Coleman, R.G., 2003. The crustal structure from the Altai Mountains to the Altyn Tagh fault, northwest China, *J. geophys. Res.,* **108,** 2322, doi:10.1029/2001JB000552.

Wei, S. *et al*., 2010. Regional earthquakes in northern Tibetan Plateau: implications for lithospheric strength in Tibet, *Geophys. Res. Lett.,* **37,** L19307, doi:10.1029/2010GL044800.

Weislogel, A., 2008. Tectonostratigraphic and geochronologic constraints on evolution of the northeast Paleotethys from the Songpan-Ganzi complex, central China, *Tectonophysics,* **451,** 331–345, doi:10.1016/j.tecto.2007.11.053.

Wessel, P. & Smith, W.H.F., 1991. Free software helps map and display data, *EOS, Trans. Am. geophys. Un.,* **72,** 441, 445–446.

Wu, Z., Ye, P., Barosh, P.J., Hu, D., Zhao, W. & Wu, Z., 2009. Late Oligocene–Early Miocene thrusting in southern East Kunlun mountains, northern Tibetan plateau, *J. Earth Sci.,* **20,** 381–390, doi:10.1007/s12583-009-0031-2.

Yin, A. & Harrison, T.M., 2000. Geologic evolution of the Himalayan-Tibetan orogen, *Annu. Rev. Earth planet. Sci.,* **28,** 211–280.

Yin, A., Dang, Y., Zhang, M., McRivette, M.W., Burgess, W.P. & Chen, X., 2007. Cenozoic tectonic evolution of Qaidam Basin and its surrounding regions (Part 2): wedge tectonics in southern Qaidam Basin and the Eastern Kunlun Range, in *Whence the Mountains? Inquiries into the Evolution of Orogenic Systems: a Volume in Honor of Raymond Price,* Geol. Soc. Am. Spec. Paper 433, pp. 369–390, eds Sears, J.W., Harms, T.A. & Evenchick, C.A., Geological Society of America, Boulder, CO, doi:10.1130/2007.2433(18).

Yin, A., Dang, Y.-Q., Zhang, M., Chen, X.-H. & McRivette, M.W., 2008. Cenozoic tectonic evolution of the Qaidam basin and its surrounding regions (Part 3): structural geology, sedimentation, and regional tectonic reconstruction, *Bull. geol. Soc. Am.,* **120,** 847–876, doi:10.1130/B26232.1.

Yue, H. *et al*., 2012. Lithospheric and upper mantle structure of the northeastern Tibetan Plateau, *J. geophys. Res.,* **117,** B05307, doi:10.1029/2011JB008545.

Zandt, G. & Ammon, C.J., 1995. Poisson's ratio of Earth's crust, *Nature,* **374,** 152–155.

Zelt, C.A. & Smith, R.B., 1992. Seismic traveltime inversion for 2-D crustal velocity structure, *Geophys. J. Int.,* **108,** 16–34.

Zelt, C.A. & Barton, P.J., 1998. Three-dimensional seismic refraction tomography: a comparison of two methods applied to data from the Faeroe Basin, *J. geophys. Res.,* **103,** 7187–7210.

Zhang, Z. & Klemperer, S.L., 2005. West-east variation in crustal thickness in northern Lhasa block, central Tibet, from deep seismic sounding data, *J. geophys. Res.,* **110,** B09403, doi:10.1029/2004JB003139.

Zhang Z., Klemperer S., Bai Z., Chen Y. & Teng, J., 2011. Crustal structure of the Paleozoic Kunlun orogeny from an active-source seismic profile between Moba and Guide in East Tibet, China, *Gondwana Res.,* **19,** 994–1007, doi:10.1016/j.gr.2010.09.008.

Zhao, W. *et al*., 2001. Crustal structure of central Tibet as derived from project INDEPTH wide-angle seismic data, *Geophys. J. Int.,* **145,** 486–498.

Zhao, W.-L. & Morgan, W.J., 1987. Injection of Indian crust into Tibetan lower crust: a two-dimensional finite element model study, *Tectonics,* **6,** 489–504.